Numerical Assessment of Ozone Addition Potential in Direct Injection Compression Ignition Engines

Vincent Giuffrida, Michele Bardi, Mickael Matrat, Anthony Robert, Guillaume Pilla

HAL Id: hal-03586133
https://ifp.hal.science/hal-03586133

Numerical Assessment of Ozone Addition Potential in Direct Injection Compression Ignition Engines

Vincent Giuffrida[1], Michele Bardi[1], Mickael Matrat[1], Anthony Robert[1], Guillaume Pilla[1]

[1] **IFP Energies nouvelles, 1 et 4 avenue de Bois-Préau, 92852 Rueil-Malmaison, France ; Institut Carnot IFPEN Transports Energie**

Abstract

This paper aims at taking into account the chemistry of O_3 in a 3D CFD simulation of compression ignition engine with Diesel type combustion for low load operating points. The methodology developed in this work includes 0D homogeneous reactors simulations, 3D RANS simulations and validation regarding experimental results. The 0D simulations were needed to take into account O_3 reactions during the compression stroke because of the high reactivity of O_3 with NO and dissociation at high temperature. The values found in these simulations were used as an input in the 3D model to match the correct O_3 concentration at fuel injection timing. The 3D simulations were performed using CONVERGE^{TM} with a RANS approach. Simulations reproduce the compression/expansion stroke after the intake valve closure to focus on the impact of O_3 on the fuel auto ignition. The comparison between numerical and experimental results demonstrates that the proposed methodology is able to capture correctly the impact of O_3 addition on ignition delay and on heat release. Moreover, the analysis of the data enables to better understand the fundamental processes driving O_3 impact in a CI engine. In particular, using 0D simulations, the plateau effect observed experimentally when increasing O_3 concentration is attributed to O_3 thermal decomposition and reaction with NO during the compression stroke. Also, 3D CFD results showed that O_3 impact is observed mainly during LTHR phase and does not affect the topology and the propagation of the flame inside the combustion chamber.

1 Introduction

Compression ignition engines are the optimal choice in terms of efficiency providing lower CO_2 emission than conventional spark ignition engines. However, the increasing restrictions in Euro norms push researchers to investigate new combustion approaches. In particular, conventional diesel combustion (CDC) is limited by the NOx-soot trade-off, which eventually hinders the simultaneous reduction of the two pollutants. To fulfill emissions regulations, Diesel vehicles have to be equipped with costly after treatment systems [1].

An effective solution to break the NOx-soot trade-off, while keeping high thermodynamic efficiency, is the low temperature combustion approach (LTC). LTC can be reached with many strategies such as homogeneous charge compression ignition (HCCI) [2–4] or partially premixed combustion ignition (PCCI) [5,2]. Despite the global in-cylinder equivalence ratio in CDC is lower than the unit, most of the pollutants are caused by local heterogeneities which are responsible for soot ($\varphi > 2$) and NOx formation (T>1800K). Exhaust Gas Recirculation (EGR) dilution strategy is the most effective to reduce combustion temperature and therefore NOx formation. However, the reduced oxygen availability causes significant degradation of soot oxidation, resulting in an increase in particulate emissions [6,7].

Since the common goal of LTC strategies is to improve the local air-fuel mixture to reduce both local temperature and equivalency ratio, chemical control of fuel auto-ignition can play an important role [8]. While in conventional CDC, fuel ignition is primarily determined by the injection timing, in LTC strategies a longer time is required to ensure a good mixing between the fuel and the cylinder gases and to reduce the local equivalence ratio. The timing of ignition event enable to control the local mixture at the time of combustion. At these conditions, injection strategy might not be

sufficient to control the combustion phasing [9] and different approaches can be found to achieve LTC in engines, such as: spark assisted ignition [10] or ignition assisted by the injection of a high reactivity fuel [11].

Another path to control fuel auto-ignition is to add highly reactive molecules which will have an impact on the ignition chemistry. In this sense, O_3 is a very reactive molecule which has an important impact on fuel ignition, even at very small concentrations. Several publications indicate that, in HCCI conditions, O_3 can be used to reduce the ignition delay, extending the working operation range and improving the control on the combustion phasing [12,13]. Magnus and Depcik [14], demonstrated experimentally that O_3 can reduce ignition delay also in CDC combustion at low load conditions while Bardi et al[15] showed that O_3 addition at low load conditions enables to improve combustion stability and increase the maximum EGR rate for a given engine condition. Similar benefits were also found when testing the effect of O_3 in CDC with low Cetane Number (CN) fuels[15]. In general, all the studies showed that relatively low O_3 seeding in the intake flow (~100ppm) can reduce significantly the ignition delay and the engine cyclic variations[16].

While experimental evidences of the potential of O_3 can be found in the literature, its applications are empirical and no proper optimization recommendation can be found. 3D computational models, in general employed for engine optimization, are still not capable to predict properly O_3 effect due to the lack of validation data as well as the complexity of the chemistry related to O_3. Kinetic mechanisms representative of O_3-fuel interactions have been employed mostly is simplified cases (e. g. homogeneous reactor) [17]. However, it is not possible to establish a quantitative link between these results and the effect observed in a direct injection engine, because of the close interaction between spray mixing, temperature and chemistry which determine spray ignition.

This paper presents a methodology developed to include O_3 effect in a commercial 3D code (CONVERGE™ V2.4.20) and its validation on experimental data obtained in an optical single cylinder engine. The application considered in this study is a CDC case at high EGR rate and low load. The deployed strategy consists of two steps involving 0D chemistry calculations based on models available in the literature[17] and 3D calculations. Results presentation is structured into three parts. The first presents the two numerical methodologies and their validation by comparison with the literature and dedicated experimental results. The second part presents the detailed results of the 0D chemistry calculation allowing to take O_3 effect on ignition delay into account in engine 3D calculations. Finally 3D calculation results are presented and compared to experiments conducted in an optical engine. These results are then discussed to better understand O_3 effects on combustion.

2 Material and methods

2.1 Engine and operating conditions

The experimental database used for CFD results validation was obtained in a previous experimental campaign on a single-cylinder optical engine. The experimental methodology and the engine test bench is thoroughly described in [15] and the main characteristics of the engine are summarized in Table 1.

The optical engine is representative of a light duty direct-injection (DI) 4-stroke Diesel engine with central mounted injector. The system is equipped with an intake heater that enables to control the intake gas temperature and a simulated EGR (pure nitrogen) circuit to target representative oxygen concentrations of standard engines. A commercial

ozone generator (Anseros COM-AD-01) was implemented in the intake line and an ozone analyzer was installed to
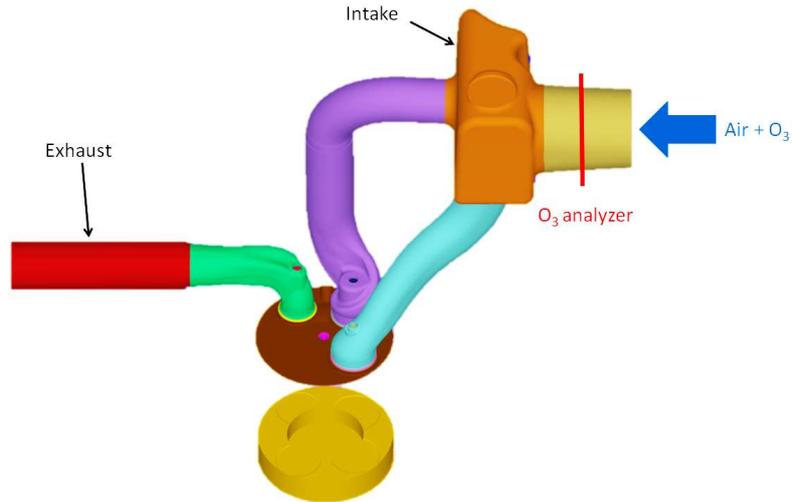
measure its concentration, as shown in

Figure 1: CAO of the simulated engine at bottom dead center showing the intake and exhaust pipes, the cylinder head and the piston bowl.

. One particularity of this engine is to have a modular configuration allowing to install optical accesses or to replace them with metallic parts. The configuration used in this study to conduct the modeling work implies only a transparent piston access. This configuration tolerates relatively high-loads and continuous firing mode. It also provides representative thermal conditions of a conventional single cylinder diesel engine, and therefore accurate combustion analysis [18].

Table 1: Single cylinder optical engine main characteristics

|	
Number of cylinders	1
Cycle	4-stroke
N. of intake valves	2
N. of exhaust valves	1
Combustion chamber	Flat bowl
Bowl diameter	48 mm
Cylinder head type	Flat
Displacement	499 cm^3
Bore	85 mm
Stroke	88 mm
Connecting rod length	145 mm
Swirl at bottom dead center	1.1
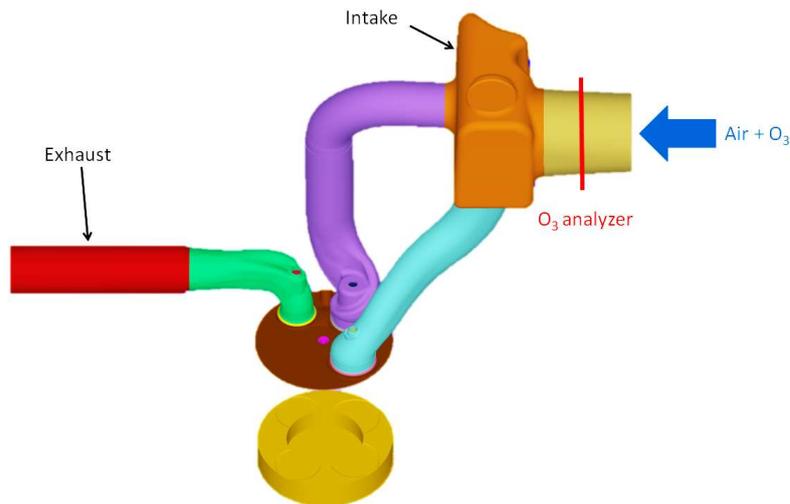
Figure 1: CAO of the simulated engine at bottom dead center showing the intake and exhaust pipes, the cylinder head and the piston bowl.

The experimental study previously conducted demonstrated that ozone has an impact on auto-ignition delay only for low load operating point with high EGR rate [15]. Thus, low load point at medium speed (3 bar IMEP at 2000 rpm) with 40% EGR was chosen. The initial average intake temperature and pressure were respectively 307 K and 1.05 bar. In this condition, an early injection at -26 CAD before top dead center (TDC) was chosen to optimize the combustion phasing without O_3. A EU-standards diesel fuel was used (B7) with an overall equivalence ratio of 0.65 and a variation of O_3 concentration at the intake from 0 to 178 ppm was performed. The O_3 effect on auto-ignition delay (t_{AI}) is presented in Figure 2 for the in cylinder pressure and the apparent heat release rate (HRR). A reactivity boost is observed through a t_{AI} reduction with an earlier combustion phasing and an increase of maximum pressure around 10 bar with 70ppm of O_3 injected at the intake ($O_{3,int}$ 70ppm). This effect is attributed to the presence of O_3 inside the cylinder and the consequent formation of radical O. These radicals interact with fuel and reduce the reactions activation energy. This aspect is better described in the next section and detailed in [13]. Also, a plateau effect appears for O_3 concentration above 100 ppm. These experimental results will serve as a reference for 3D modeling strategy development.
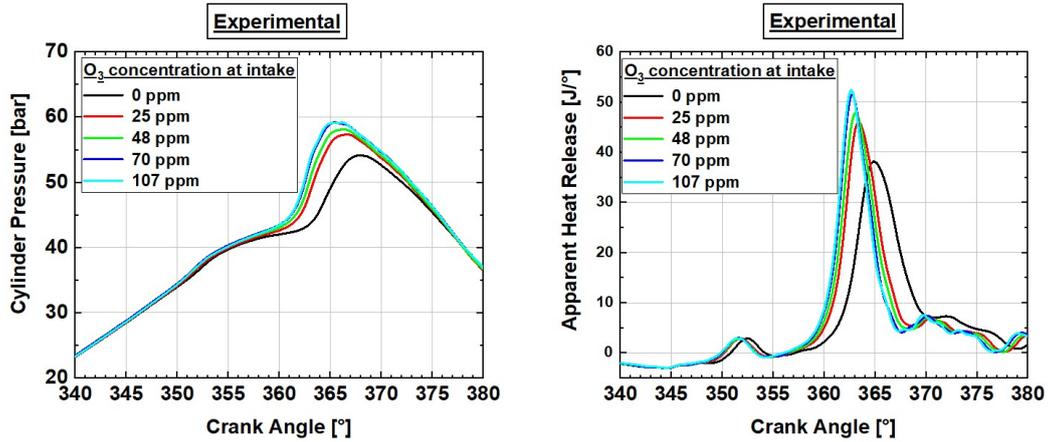
Figure 2: Experimental pressure and apparent HRR for 5 ozone concentration initially introduce

2.2 CONVERGE™ description and numerical strategy

CFD simulations are performed with CONVERGE™ adapting the code version v2.4 to account for O_3 reactivity. Three complete cycles are simulated to provide numerical convergence. The computational domain contains the full geometry (combustion chamber, intake pipe and plenum and exhaust pipe). All the geometrical details of the bottom part of the cylinder head are also included (injector geometry, intake and exhaust valve bottom). The grid is automatically generated by a cut-cell method implemented in CONVERGE™ which is coupled with automatic mesh refinement (AMR) [19]. This approach avoids time-consuming mesh generation, which is of particular interest in the engine framework due to the moving boundary layers and complex geometries.

Simulations are performed in the RANS phase-averaged framework. Classical eddy-viscosity concept is assumed for closing the Reynolds tensor, and the turbulent viscosity is computed from the RNG k-ε model [20]. The wall heat transfer is ensured by the O'Rourke and Amsden model [21].

The compressible unsteady formulation of Navier-Stokes equations is solved owing to the iterative PISO method [22]. The pressure and the density are coupled according to an ideal gas state equation. Regarding the spatial schemes, the momentum equation is discretized with a second order central scheme while the first order upwind scheme is used for the other balance equations for species and turbulence. The time step is variable and satisfies a maximal convective CFL number below 1 and a maximal CFL number based on speed of sound below 100.

Liquid fuel injection is modeled by using the Lagrangian Particle formalism. The spray is described as a collection of discrete droplets and those sharing the same properties are combined in single parcels which are tracked using the Lagrangian approach. The droplet drag, which relies to the feedback of the gas phase on the liquid one, is closed by a dynamic drag model accounting for the distortion of the droplets. The atomization process is modeled by the modified Kelvin-Helmholtz Rayleigh-Taylor (KH-RT) model [19,23,24]. The latter represents the instabilities mechanisms leading respectively to the primary and secondary spray breakup. The production of child parcels is enabled which implies that the primary breakup KH model allows new parcels to be produced from the primary breakup. The modified KH-RT model relies on the application of secondary RT break-up only to these child parcels. The rate of change of droplet diameter due to evaporation is computed according to Frossling correlation [25].

Combustion is modeled by the 3-Zones Extended Coherent Flame Model (ECFM3Z) model [26]. This model is based on ECFM [27], which is dedicated to combustion processes dominated by flame propagation in perfectly or partially mixed media. ECFM3Z is an extension of ECFM to heterogeneous combustion, and it is able to represent all the combustion regimes encountered in Diesel combustion. To model the diffusion flame and the associated mixing process, each computational cell is split into three mixing zones: a first zone with only fuel, a second zone with only air and residual gases, and a third one where the components of the first and second zone are mixed. ECFM is then applied in the third zone (mixed zone). A mixing model allows progressive mixing of the fuel with the in cylinder gas. This mixing model takes into account the turbulence effect on the combustion through the mixing terms of the ECFM3Z specific transport equation [26] that are function of the turbulence time scale τ_m. The auto-ignition process, which is of pivotal importance

in Diesel combustion, occurs in the mixed zone in ECFM3Z model. This process is modeled by the Tabulated Kinetics of Ignition (TKI) model [28,29] which enables to include detailed chemistry effects with small computational costs. TKI is based on the tabulation of homogenous reactors for various conditions of pressure, temperature, fuel air equivalence ratio and EGR. The main difference over a classical TKI table for Diesel 3D simulations, lies in the presence and discretization of O_3 concentration inside the homogeneous reactor. In CONVERGE[TM], the solver interpolates into the table to assess the data for auto-ignition, this process requires much less computational resources than the use of a chemical solver.

Finally, a new methodology is needed to predict the O_3 mass fraction effectively present at injection timing, which will be used by the TKI table to obtain the ignition delay.

Indeed, the increase of temperature taking place during the compression stroke induces a dissociation rate of O_3 through reaction (1), causing a difference between the amount of ozone seeded at the intake ($O_{3\%, int}$) and the amount of ozone actually available at the moment of injection ($O_{3\%, inj}$). Afterwards, radical oxygen formed by O_3 dissociation can recombined to form O_2 molecule through reaction (2).

$$O_3 \rightarrow O_2 + \dot{O} \quad (1)$$

$$\dot{O} + \dot{O} \rightarrow O_2 \quad (2)$$
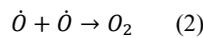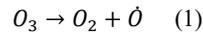
Moreover, residual gases from the previous combustion cycle contain a certain amount of nitric oxide (NO). This molecule also reacts with O_3 through reaction (3).

$$O_3 + NO \rightarrow NO_2 + O_2 \quad (3)$$

The solution of equations related to reactions (1), (2) and (3) is very important to determine the amount of O_3 available at the time of injection. However, it would affect substantially the computational cost of the 3D simulation, for a process which is, in first approximation, homogeneous. For this reason, an alternative strategy was adopted. It is schematically described in Figure 3. The first step in this strategy is to determine the concentration of ozone available at the time of injection. This is done by solving the reaction system (1), (2) and (3) in a 0D homogeneous reactor. This concentration is then used as an input variable in the TKI table for the 3D calculation.
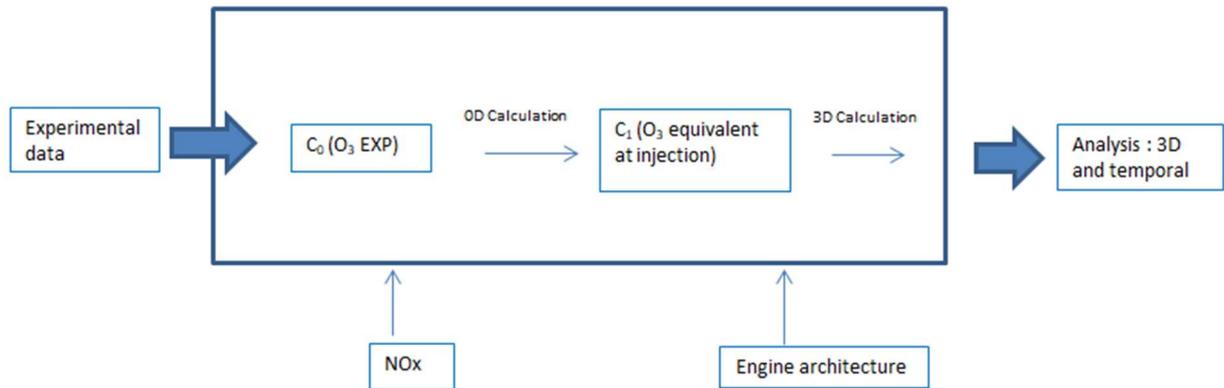

Figure 3: Global scheme of the correlation between 0D and 3D calculations

2.3 Kinetic mechanism validation

The first step of this study was the definition of a chemical kinetic mechanism process for the n-heptane fuel in combination with chemical mechanism for O_3. The mechanism has to take into account the effect of O_3 on the auto-ignition delay. The detailed mechanism for n-heptane developed by Mehl et al. [30] (referred hereafter as LLNL mechanism) was chosen as it constitutes a reference for such hydrocarbon reactivity and combined with complete O_3 block inspired from Masurier et al. [31]. The resulting mechanism thus contains global reactions for O_3 dissociation, interactions between small hydrocarbons, NO and O_3. This reaction mechanism will be referred to as modified LLNL scheme in the rest of this paper. The list of reactions for this O_3 block is presented in appendix 1.

Due to the lack of experimental data in the literature, the prediction of t_{AI} for the mechanism developed here was compared to homogeneous reactor simulations performed by Masurier et al. in a constant volume reactor [31]. The same thermodynamic conditions were used, i.e. with initial pressure of 25 bars, equivalence ratio of 0.3 and variation in initial temperature from 600 K up to 1350 K and four different ozone molar concentrations (0, 1, 10 and 45 ppm). The results are presented in Figure 4. The auto ignition delay is here defined as the time needed for the reactor to increase its temperature by 400 K.

There is good general agreement in t_{AI} predictions, both in terms of order of magnitude and parametric sensitivity. Between 1300 and 1000 K the auto-ignition delays are very similar to those obtained by Masurier et al. for the entire Y_{O_3} variation. Below 1000 K, the plateau corresponding to the negative temperature coefficient (NTC) is well reproduced for each O_3 concentration rate.

To quantify and compare the reduction in t_{AI} induced by O_3, we define the parameter R as follows:

$$R(Y_{O3}, T, P) = \frac{t_{AI}(Y_{O3}, T, P) - t_{AI}(YY_{O3,0}, T, P)}{t_{AI}(Y_{O3,0}, T, P)} \qquad (eq.\ 1),$$

Where Y_{O3} is O_3 concentration (with and $Y_{O3,0}$ = 0ppm), T and P are the initial temperature and pressure respectively. The results for a temperature of 625 K are presented in Figure 5. For an initial temperature below 700 K, a significant increase in R is observed between 0 and 1 ppm of O_3 for both Masurier and modified LLNL block scheme. R is about 0.6 for Y_{O3} = 1 ppm for both chemical schemes. On the other hand, a further increase of Y_{O3} causes a smaller increase of R, being R ≈ 0.8 for Y_{O3} = 45ppm. The same sensitivity is observed between LLNL + O_3 and Masurier's mechanism. Finally, Figure 6 presents the difference between main flame ignition delay (t_{ai}) and cold flame auto-ignition delay ($t_{ai,cf}$) with $t_{ai,cf}$ defined as the time needed to increase the temperature of the 0D reactor by 100 K. Figure 6 shows that this difference remains the same for every O_3 rate at each temperature. It implies that O_3 mainly impacts $t_{ai,cf}$. The same effects were observed experimentally showing that O_3 presence impacts mainly Low Temperature Heat Release [15].
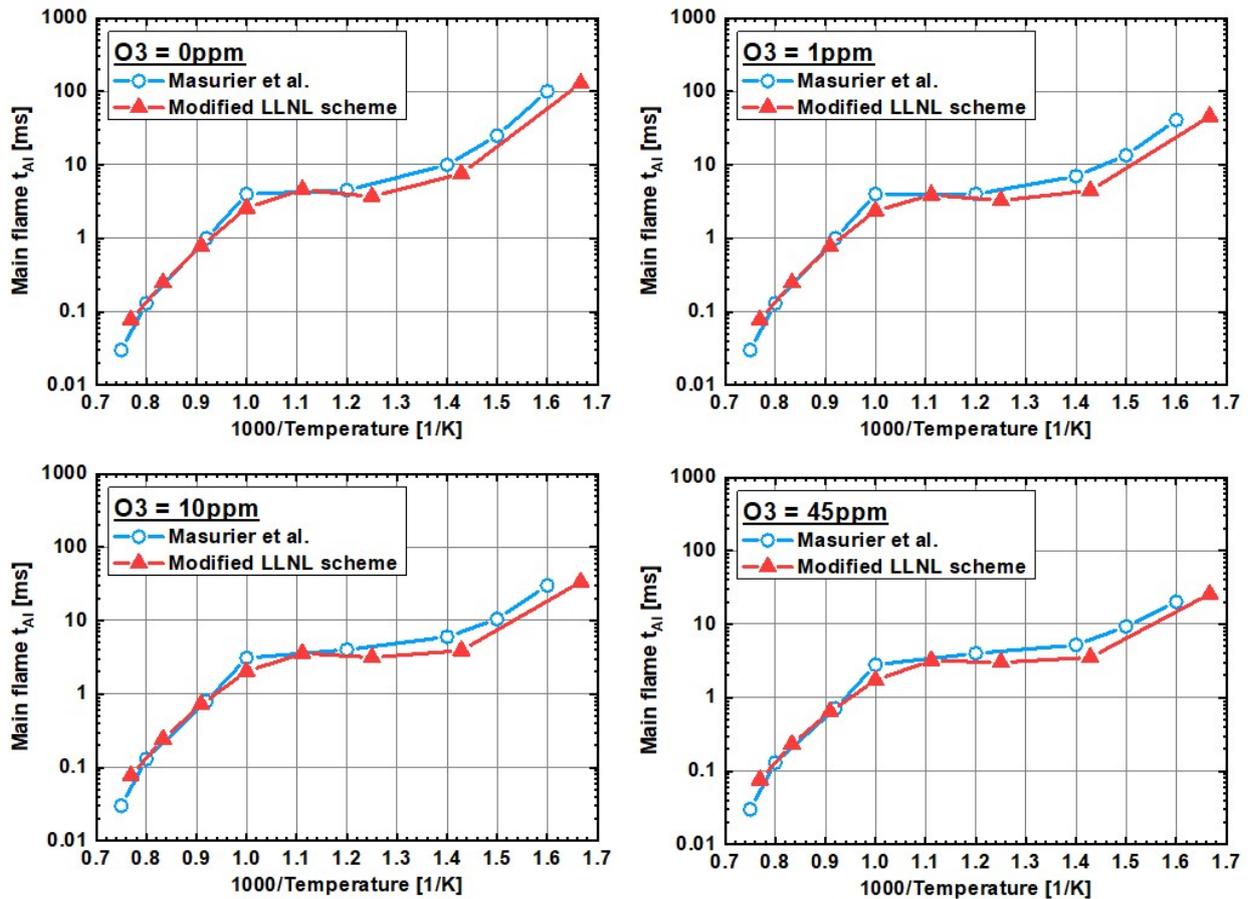

Figure 4: Comparison of t_{ai} predicted at 4 different Y_{O3} with Masurier et al. mechanism and modified LLNL scheme
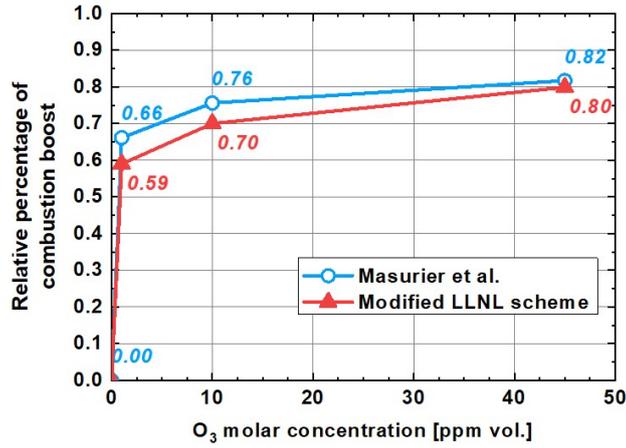
Figure 5: Comparison of ignition delay reduction (R) predicted with Masurier et al. mechanism and modified LLNL scheme
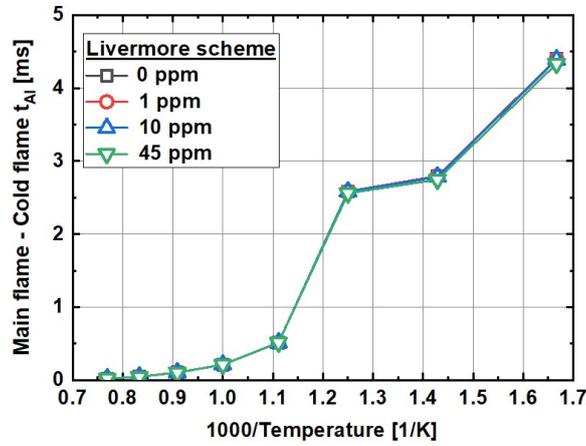

Figure 6: Comparison of t_{ai}- $t_{ai,cf}$ predicted for 4 different Y_{O3} with modified LLNL scheme3D input variable description and validation

2.4   3D input variable description and validation

The mesh used for the 3D simulations follows the same strategy as in [32] which demonstrated robust results for Diesel engine calculation. The only change is the increase of cone spray embedding by one level to limit numerical diffusivity proper to Cartesian mesh. Previous grid convergence study on both reactive and non-reactive spray by Senecal et al [33] shows mesh convergence with AMR method for mesh size below 0.25 mm. Based on these results, the following mesh strategy was adopted in this study. The base size is here set to 2.6 mm. The combustion chamber is refined during intake valve closure (IVC) period with a size of 1.4 mm and a cone spray embedding is prescribed with a cell size of 0.175 mm. A wall embedding is also prescribed on the piston and the cylinder head with a cell size of 0.175 mm. The AMR method, which enables refinement if large gradients of velocities, temperature, or n-heptane mass fraction are detected, is activated with a cell refinement down to 0.35 mm. The overall mesh inside the combustion chamber during injection is presented in Figure 7 and shows these different types of refinement.
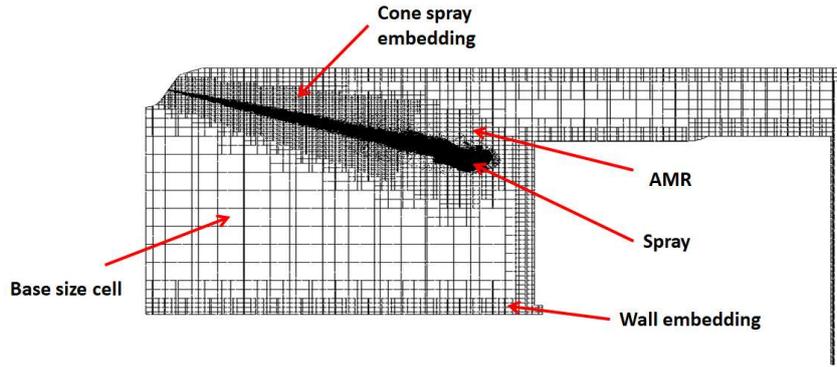
Figure 7: Mesh of the combustion chamber 3 CAD after effective beginning of injection

Regarding boundary conditions, fast measurements of pressure inside the intake pipe (before the plenum) and inside the exhaust pipe are considered. The EGR introduced at the intake is composed entirely of N_2 and represents 40% of the total intake. An injection rate characterization was realized using a Bosch tube method device [34] and was set as the boundary condition for the Lagrangian injection and breakup models. The description of the injector is presented in Figure 8. The liquid parcel injected is defined as a physical Diesel surrogate and follows the physico-chemical characteristics of a conventional B7 Diesel fuel. Once evaporated, a gaseous surrogate is used for the auto-ignition properties. This surrogate is composed of n-heptane only as this compound is a common fuel surrogate for diesel reactivity. Indeed, both have a similar CN. Finally, wall temperatures are obtained using an Amesim 0D simulation. Results are presented in Table 2.

Injector characteristics	
Injector actuator	Solenoid (Bosch CRI 2.16)
N. holes	6
Holes diameter	129 µm
Spray angle	149°
Injection pressure	800 bar
Injected mass	10 mg
Start of injection	-26 CAD aTDC
Injection duration	450 µs
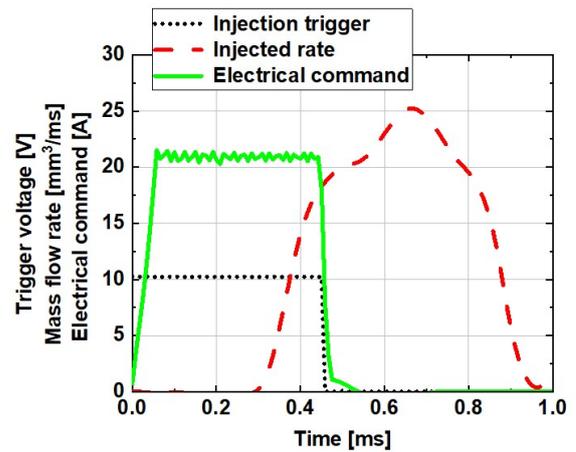
Figure 8: Injector characteristics (left) and rate of injection (right)

Table 2: Wall temperatures boundary conditions

Temperatures	
Liner	372 K
Intake	307 K
Cylinder head	428 K
Intake plenum	428 K
Piston	421 K
Exhaust	493 K

Finally, the TKI table was generated using the modified LLNL scheme presented above. The discretization detailed in Table 3 lead to 116610 homogeneous reactors that will be used in the 3D calculation strategy.

Table 3: TKI table discretization description

N_2 incorporation rate [%vol.]	0, 10, 20, 50
O3 molar rates [ppm]	0, 20, 50, 100, 200, 500
Equivalence ratio	0.1 to 3.0 (8 values)
Pressure range [bar]	1 to 200 (11 values)
Temperature range [K]	500 to 1500 (55 values)

The validation of the simulation strategy presented above was conducted in several steps. First, a 3D motored engine simulation of three cycles was realized to confirm the boundary conditions and inputs presented above. A satisfactory convergence was obtained after three cycles. The Third simulated cycle is compared to the experimental cold flow data in Figure 9. Even though a little over-estimation of the pressure increase is observed, the simulated results show good agreement with experiment.
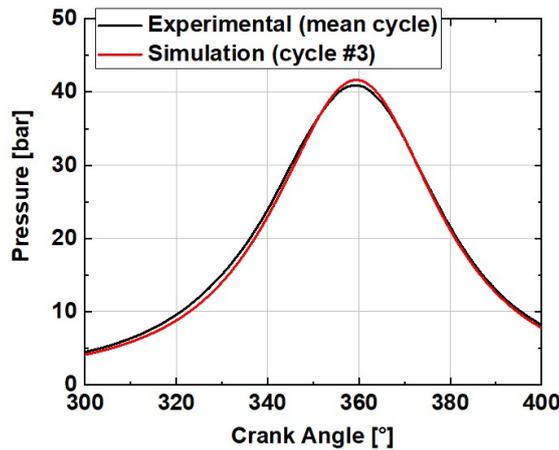

Figure 9: Simulation of three consecutive cycles of motored engine compared to motored experimental results

The following validation step consisted in activating the Lagrangian spray injection model, coupled to ECFM3Z/TKI model for combustion, for a simulation without O_3 introduced at the intake.

The operating points of interest for the current study present long initiation duration, (e.g. 20-30 CAD). Indeed the desired effect of O_3 is to shorten t_{AI} to stabilize the initiation of combustion. The first results obtained showed that the envisaged strategy led to an underestimation of t_{AI}. This was attributed to the wrong sensitivity of the simulation to the TKI table for long AI delay. Nevertheless, since the present detailed mechanism has been extensively validated in the literature, choice is made in this study to use this mechanism and to counterbalance its sensitivity at low temperature by applying a multiplication factor of 1.3 inside the TKI table, regardless of the O_3 concentration. This strategy enables to synchronize the main ignition delay with the experimental data. Therefore the TKI table trends to evaluate the relative effect of O_3 addition is preserved. The results are presented in Figure 10 for the in-cylinder pressure and the apparent HRR. A satisfactory agreement is obtained with the experimental results. Indeed, a good match is obtained for the compression phase, auto-ignition delay and exhaust phase. The only discrepancy concerns the peak of pressure with a 6 % under-estimation compared to the experimental result. Hypothesis to explain this disparity could be the blow-by flow rate which is not well characterized in optical engines or the amount of unburnt hydrocarbons. However, considering that the first order phenomena impacting combustion boost by O_3 is the reduction of t_{AI}, it was not further investigated in the present study and will be addressed in future work.
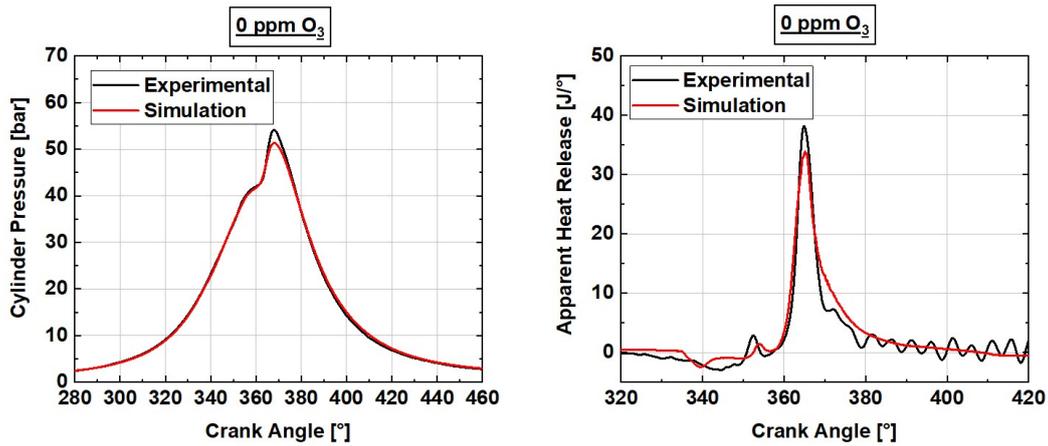
Figure 10: Comparison between simulation and experimental results for engine operation without O_3

3 Results and discussion: 0D Simulation

3.1 O_3 concentration evolution during the compression stroke

The methodology linking 0D and 3D calculations previously detailed provides an O_3 equivalent concentration at injection timing noted $O_{3\%, inj.}$ This value ensures the correct ignition time reduction in the 3D simulations. Motored engine cycle was simulated using CHEMKIN 0D. The initial conditions were set to have the same compression ratio of 16.6 and same initial thermodynamic conditions as the engine used in experiments. A range between 1 ppm and 500 ppm of O_3 concentration at the intake was investigated. The variation of O_3 and atomic oxygen concentrations during the cycle are presented in Figure 11. Ozone molar fraction remains constant up to a certain crank angle position. Afterwards, O_3 concentration drops quickly and simultaneously atomic oxygen is formed through reaction (1). Atomic oxygen being unstable, its molar fraction then decreases rapidly through the recombination reaction (2).
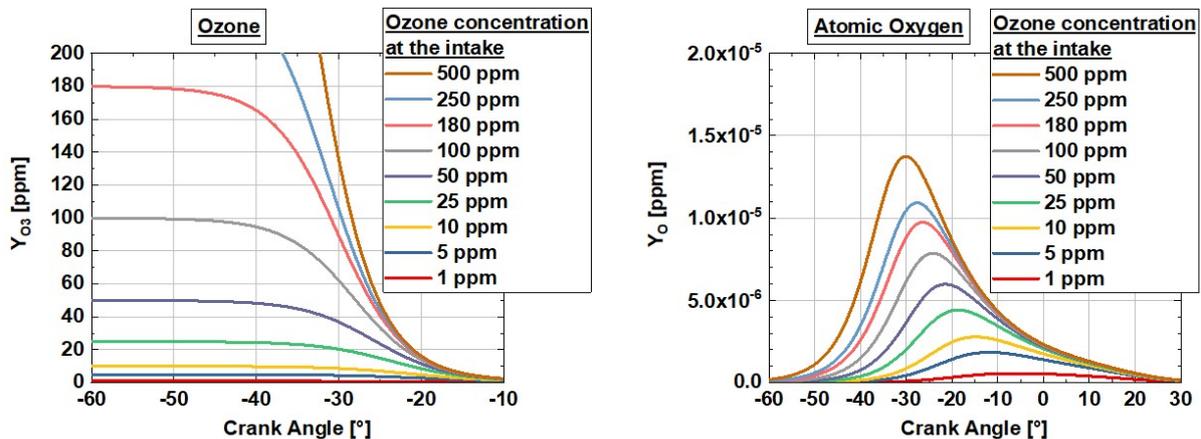
Figure 11: Molar concentration of O_3 (left) and atomic oxygen (right) in a motored cycle for different O_3 molar concentration at the intake.

During engine tests, injection timing occurred at 26 CAD before top dead center. Even at this early timing, the concentration of O_3 has already started to drop. For instance, Figure 11 shows that from 500 ppm of O_3 at the intake only 60 ppm remains at injection timing, which represents only 12% as compared to the $O_{3\%, intake}$.

To quantify this drop in O_3 concentration, the O_3 and atomic oxygen concentrations at injection timing are plotted as a
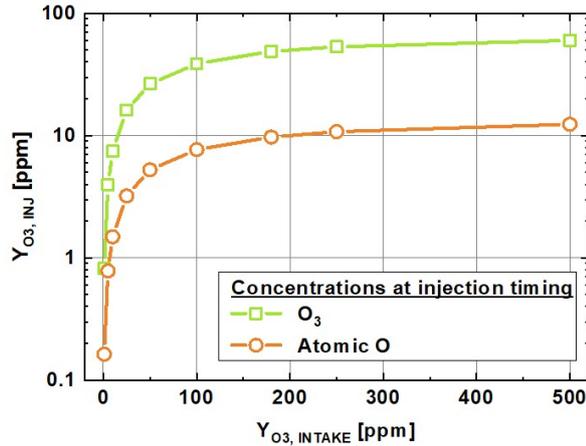
function of $O_{3\%,\ intake}$ in

Figure 12. These two plots show a plateau in O_3 and atomic oxygen concentrations at injection timing when $O_{3\%\ intake}$ is increased. This result implies a limitation in the marginal increase of O_3 at injection timing. This correlates well with the experiments (cf. Figure 2).
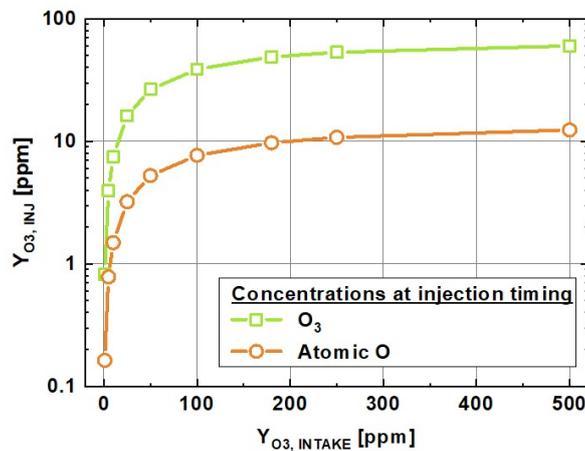
Figure 12: 0D simulation results for concentration of O_3 (green) and atomic oxygen (brown) remaining from O_3 thermal dissociation at injection timing at -26 CAD (injection timing) in motored conditions.

3.2 NO effect on Ozone dissociation

As seen earlier, O_3 concentrations can be greatly affected by the presence of NO in the chamber through reaction (3). Indeed, thanks to measurements in the exhaust line during experimental tests, NO concentration has been evaluated around 30 to 40 ppm in the combustion chamber, after fresh gases mix with residual gases. To evaluate the left-over O_3 concentration after compression, 0D simulations were performed for an initial concentration of O_3 of 100ppm. The results presented in Figure 13 therefore take into account both O_3 thermal dissociation (reaction 1) and NO effect (reaction 3). The figure clearly indicates that the presence of few dozen ppm of NO implies an important reduction of O_3 concentration at injection timing. Consequently, it amplifies the plateau effect generated by the thermal dissociation of O_3 and observed in Figure 13 showing that for engine-like conditions, with 100 ppm of O_3 introduced at the intake, only 0.1 to 2 ppm of O_3 remains inside the combustion chamber to produce a boosting effect.
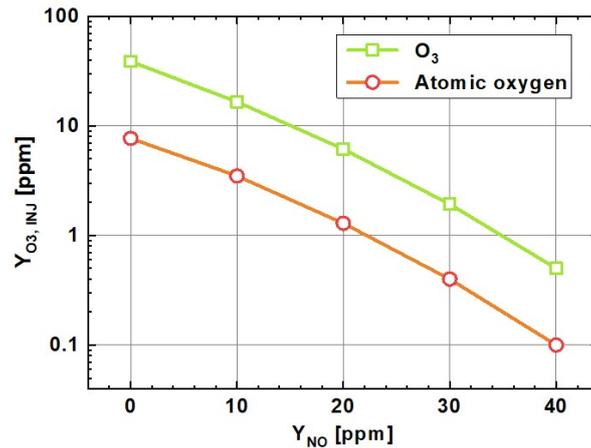
Figure 13: : 0D simulation results for concentration of O_3 (green) and atomic oxygen (brown) at injection timing for different NO concentration at IVC and $O_{3, intake}$ 100 ppm in motored conditions.

Following the methodology previously described, an estimation of the $O_{3\%,inj}$ was obtained for each value of $O_{3,int}$ and set as intake boundary condition. E.g., O_3 concentration obtained for 107 ppm at the intake was around 1 ppm at injection fuel timing. The available O_3 concentration at injection timing are represented in Figure 14.
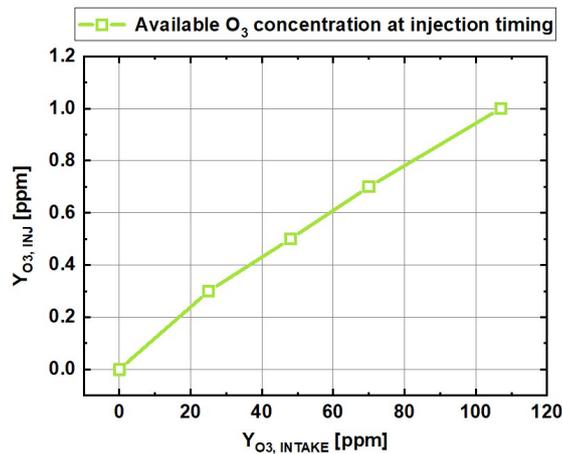

Figure 14: Estimation of O_3 concentration at injection timing taking into account thermal dissociation and NO effect on initial O_3 concentration at the intake

4   3D simulation and comparison to engine experimental results

4.1   Combustion analysis results

In this section results from 3D CFD simulation are presented together with a comparison to experimental data. Figure 15 and Figure 16 present computational and experimental results for in-cylinder pressure and apparent HRR, respectively. Simulation results are presented on the left while experimental results are presented on the right. It can be seen that the O_3 effect on combustion initiation is well captured by the numerical simulations. The ignition delay reduction was quantified by measuring the advance of the HRR maximum phasing when compared to the reference no O_3 case. In CFD simulation the HRR peak advance for 25 and 70 ppm $O_{3,int}$ is respectively 1.27 CAD (equivalent to 105 µs) and 2.54 CAD (equivalent to 211 µs) while, experimentally, the reduction was 1.5 CAD (equivalent to 125 µs) for 25 ppm $O_{3,int}$ and 2.1 CAD (equivalent to 175 µs) for 70 ppm $O_{3,int}$.Nevertheless, two discrepancies can be observed. First, the plateau effect is not well reproduced above 70 ppm of O_3 at the intake. Indeed, this plateau has been explained above using chemistry simulations, however the prediction of the ozone concentration is not accurately determined. To investigate this aspect more data on the experimental conditions are needed, i.e. gas temperature and residual gas

composition. The second discrepancy concerns the combustion development. In Figure 16, a second peak in aHRR can be observed in numerical simulations after 364 °C.A. (c.f. red arrow). Since no O_3 is left at this timing, it cannot be attributed to its effect. Indeed, the analysis of the 3D simulations revealed that this peak was due to spots of AI in the squish zone. This difference could be related to discrepancies in fuel mixing field calculations, which might over-predict the amount of fuel in the squish region.
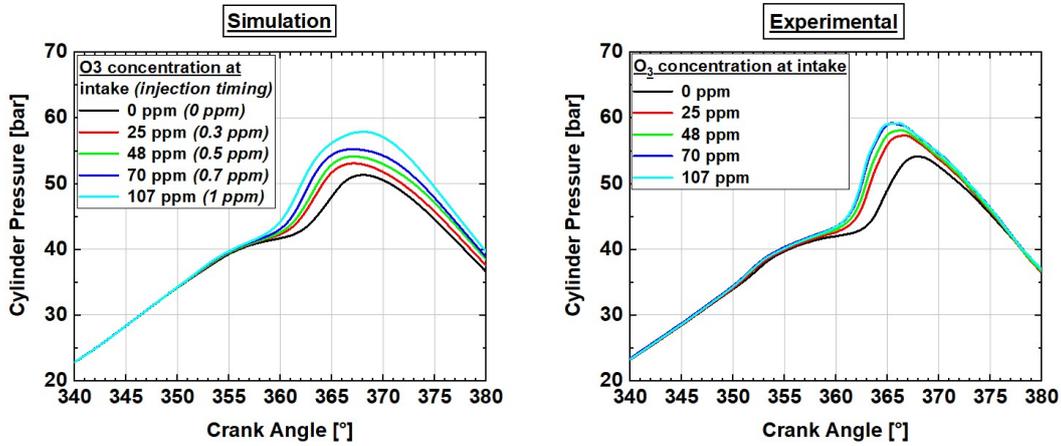
Figure 15: Numerical (left) and experimental (right) in-cylinder pressures for several $O_{3n\ int}$ values.

Figure 16: Numerical (left) and experimental (right) apparent HRR for several $O_{3,\ int}$ values.

To evaluate the ability of the numerical strategy developed in this study, the analysis was focused on combustion characterization through the pressure amplitude increase by calculating the maximum pressure reached (P_{max}) and the angular position at which it is reached (Θ_{Pmax}). Figure 17 and Figure 18 show the relative variation on P_{max} and Θ_{Pmax}, respectively. For both parameters the reference value is taken at $O_{3,int} = 0ppm$. Experimental and numerical results show good agreement in their sensitivity to $O_{3,int}$. For P_{max} and Θ_{Pmax}, the general trends are well captured. Nevertheless, the plateau effect is not as well reproduced. As mentioned earlier, higher precision on NO concentration and therefore $O_{3,inj}$ value are needed to draw an overall conclusion.
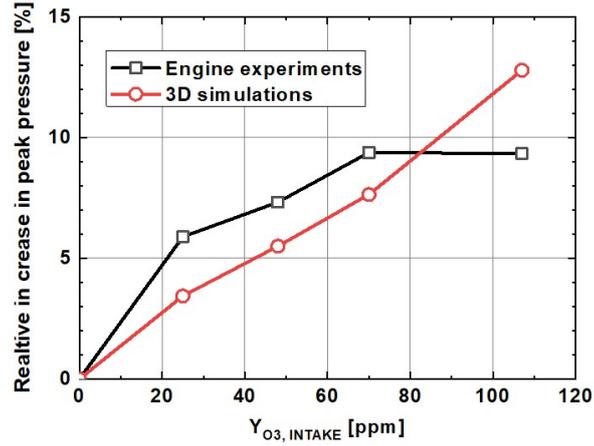
Figure 17: Comparison between experimental and numerical results for O_3 impact on maximum in-cylinder pressure. The reference value obtained at $O_{3,int}$ = 0ppm.
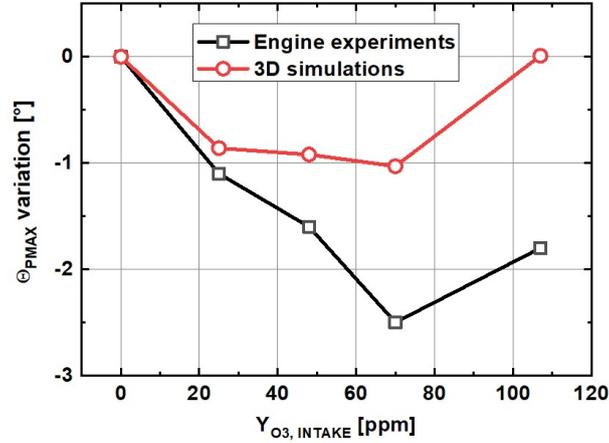
Figure 18: Comparison between experimental and numerical results for O_3 impact on Θ_{Pmax}. The reference value obtained at $O_{3,int}$ = 0ppm.

4.2 O_3 impact in the 3D domain

Thanks to the 3D data generated with the simulation, the combustion process can be analyzed regarding the great heterogeneities encountered in the chamber. Figure 19 presents a comparison of these 3D data between 0 ppm (left) and 70 ppm (right) $O_{3\%,int}$. In this figure each point in this scatter plot graph represents a specified cell of the 3D computational domain. In these graphs, the x-axis represents the local equivalence ratio (φ) in the cell, the y-axis the local temperature in the cell and each point representing a cell are then colorized by the auto-ignition progress variable (λ) in order to compare the spectrum where AI occurs.

The auto-ignition progress variable is defined as the fuel mass proportion having burnt in auto-ignition mode and it is linked to the premixed flame progress variable $\widecheck{\widetilde{c}}_\Sigma$ and the total progress variable $\widecheck{c}$ in Equation 2.

$$\lambda = \frac{\widecheck{c} - \widecheck{\widetilde{c}}_\Sigma}{1 - \widecheck{\widetilde{c}}_\Sigma} \qquad \textit{(eq. 2)}$$

λ ranges from 0, before any reaction takes place, to 1 if all the fuel mass have been burnt in auto ignition combustion mode. The figure presents the results for the initial phase of ignition (low temperature heat release LTHR) on the top and the second phase of the ignition (high temperature heat release, HTHR) at the bottom. In this case the two ignition phases are identified arbitrarily basing on the maximum value of the progress variable in the entire domain ($\lambda < 0.1$ in the LTHR) and the modest increase in temperature. Both phases (LTHR and HTHR) are compared at close relative heat release level. It can be observed that the main effect of O_3 on AI occurs during LTHR period. Indeed with 70 ppm $O_{3\%,}$ $_{intake,}$ the spectrum of φ and temperature in which the AI occurs is greatly extended from 1.5 to 2.5 φ without O_3 to 0.5

15

to 2.5 φ (red circle pointed by the red arrow in Figure 16). Contrary to the LTHR phase, the spectrum of the HTHR phase is not impacted by O_3. Therefore it can be concluded that the impact of O_3 on auto-ignition delay is mainly observed during LTHR period. The same characteristics have been observed experimentally with CH_2O LIF showing that O_3 presence increases CH_2O emissions and thus mainly impacts LTHR combustion phase [1].
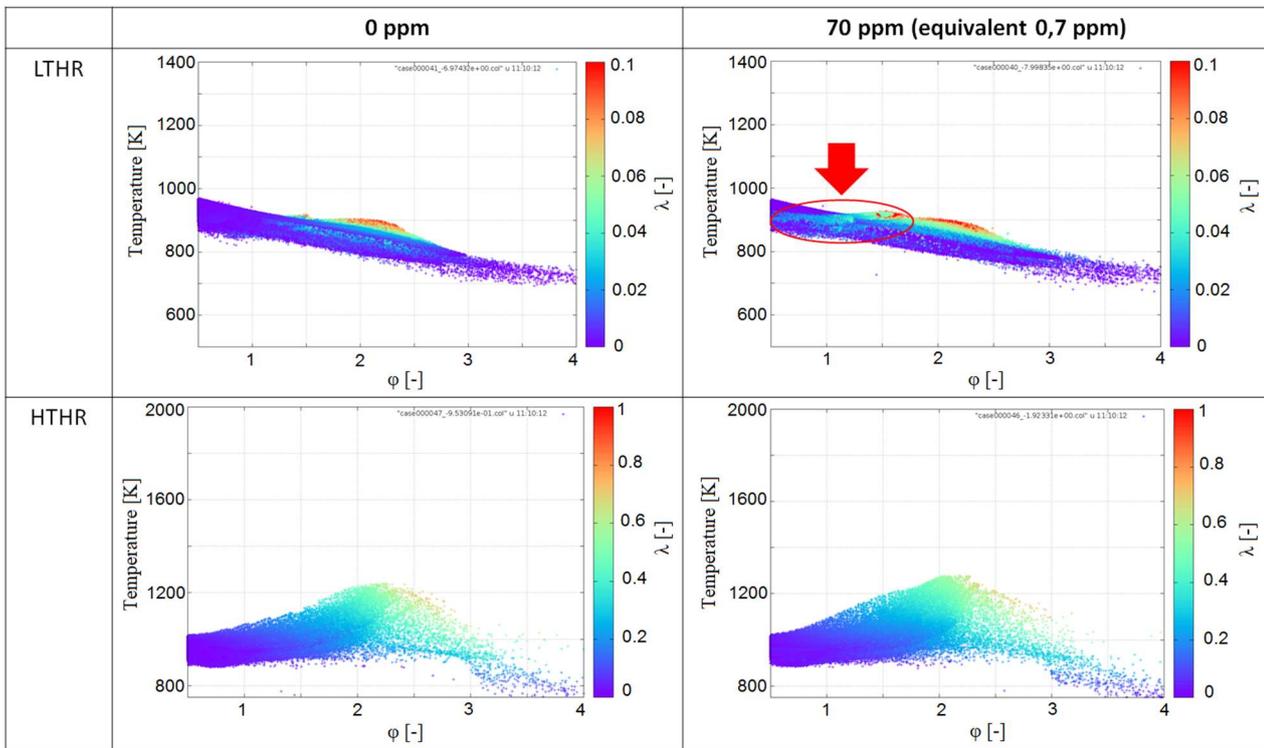
Figure 19: Scatter plot representing the progress variable of AI function of temperature and φ for HTHR and LTHR phase at $O_{3,inj}$=0 ppm and $O_{3,inj}$=0.7 ppm

Finally, to observe the location of AI and the topology of the flame inside the combustion chamber, two types of iso-surface were generated for the AI progression variable: one for the LTHR with a cut off value of 5% and another one for the HTHR with a cut off value of 20%. Figure 20 and Figure 21 compare 0 ppm and 70 ppm at the intake for LTHR and HTHR respectively. Data output are extracted at a same heat release timing. Due to the long AI delay, the flame is mainly located at the center of the piston bowl. A first remark concerns the flame propagation and topology that is completely different compared to a quasi-steady Diesel combustion plume as observed by [35]. This fact is related to the high EGR dilution characterizing the case tested which enhances fuel mixing with the surrounding fuel and increases simultaneously the flame AI delay. The second observation concerns the development and the topology of the flame that do not seem to be impacted by O_3 addition. This aspect suggests that O_3 only affects t_{AI} but not the flame topology and propagation.
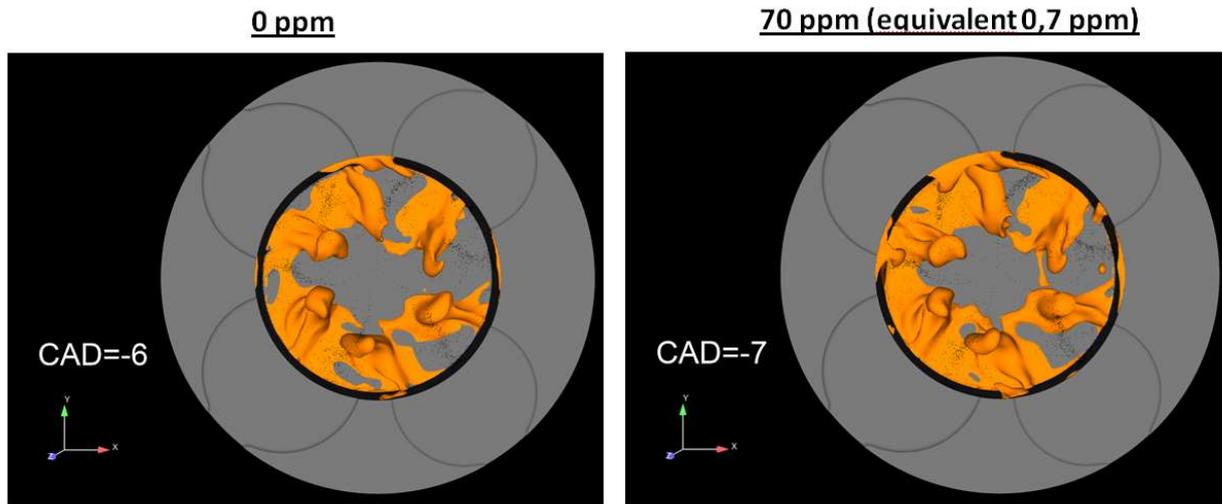
Figure 20: Iso surface of λ (5 % cutoff) comparison at iso HRR for 0 ppm (left) and 0.7 ppm (right)
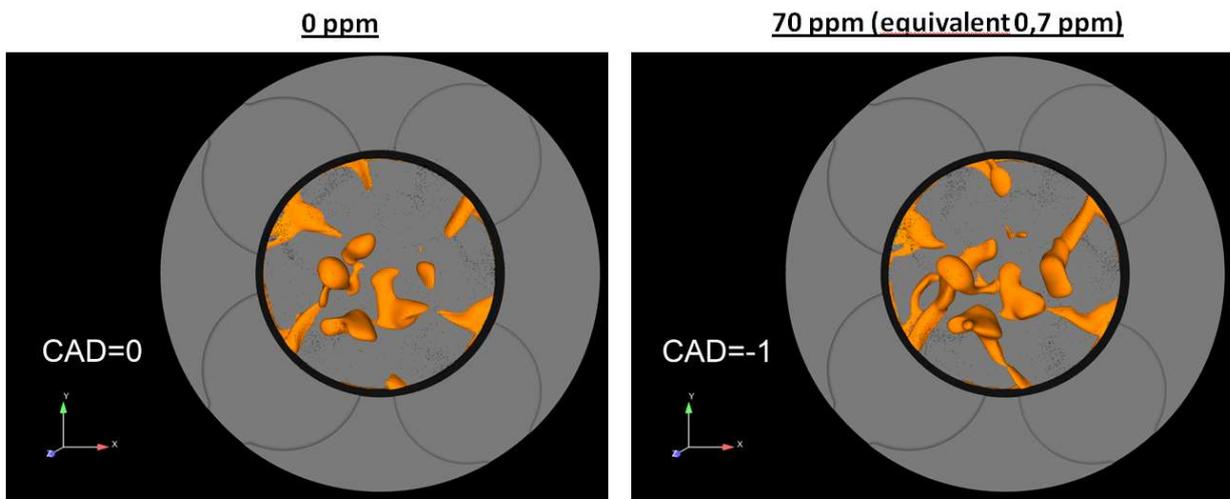
Figure 21: Iso surface of λ (20 % cutoff) comparison at iso HRR for 0 ppm (left) and 0.7 ppm (right)

5   Conclusion

This paper presents a methodology to take into account the effect of O_3 in a compression ignition engine using 3D simulation. A 3D simulation code (CONVERGE™ V2.4.20) was employed to replicate experiments carried out in a compression-ignition single-cylinder optical engine at low load conditions. The methodology includes a 0D simulation approach to include the O_3 chemistry before injection (e.g. O_3 dissociation and interaction with NO). This solution enables to calculate the correct O_3 concentration at the injection timing (which eventually interacts with the fuel) without any additional computational cost. The methodology developed enables to reproduce the experimental results with a good match in terms of O_3 impact on fuel ignition and combustion phasing. The sensitivity to O_3 concentration was also verified with satisfactory results.

The calculations carried out also make it possible to gain understanding on the phenomenology of O_3 effects in a compression ignition engine:

- It has been previously observed experimentally that the marginal effect of an increasing concentration of O_3 at intake tends to zero, causing a plateau effect. The 0D simulations showed that as O_3 concentration at the intake is increased, the O_3 dissociation becomes faster and limits the marginal increase of O_3 availability at the injection

timing. This fact indicates that the plateau observed experimentally is mainly related to the chemistry taking place before the injection and to the O_3 dissociation.

- The presence of NO molecules in the residual gases causes an important reduction of O_3 concentration at the injection timing. This aspect can significantly reduce the global effect of O_3 on combustion.
- O_3 mainly affects the ignition phase in particular reducing the delay of the first stage of ignition (low temperature heat release). Calculations also showed that no discernible impact can be observed on flame topology or in flame propagation.

This work, proved the applicability of the methodology for compression ignition engine case. However, further progress could be made on the chemical kinetic aspect. Indeed some improvement are required to allow good predictability of the ozone concentration at injection timing. Fundamental experiments are required to accurately take into account thermal dissociation and O_3/NOx reactions. This would enable the prediction of the plateau effect.

Regarding the results obtain with a direct injection engine, further application can be foreseen. For instance, O_3 additions would provide a great opportunity to control gasoline compression ignition engine. To proceed this way, some work is needed to evaluate the potential of O_3 with the chemistry of the specific fuels required for these combustion strategies.

6 Acknowledgments

7 Nomenclature

CAD	Crank angle degree
CFD	Computational fluid dynamics
CN	Cetane Number
ECFM3Z	3-Zones Extended Coherent Flame Model
EGR	Exhaust gas recirculation
HRR	Heat release rate
HTHR	High temperature heat release
IVC	Intake valve closure
LIF	Laser induced fluorescence
LLNL	Laurence Livermore National Lab.
LTHR	Low temperature heat release
NTC	Negative temperature coefficient
$O_{3,int}$	O_3 concentration in the intake flow
$O_{3\%, inj}$	O_3 concentration at the injection timing
TKI	Tabulated Kinetics of Ignition
t_{ai}	Auto ignition delay
$t_{ai,cf}$	Cool Flames auto-ignition delay (LTHR phase)
λ	Progress variable

8 References

1. Miles PC and Andersson Ö. A review of design considerations for light-duty diesel combustion systems. *International Journal of Engine Research* 2016; 17: 6–15.
2. Ji C, Dec JE, Dernotte J and Cannella W. Effect of Ignition Improvers on the Combustion Performance of Regular-Grade E10 Gasoline in an HCCI Engine. *SAE International Journal of Engines* 2014; 7: 790–806.

3. Bendu H and Murugan S. Homogeneous charge compression ignition (HCCI) combustion: Mixture preparation and control strategies in diesel engines. *Renew. Sust. Energ. Rev.* 2014; 38: 732–746.
4. Paykani A, Kakaee A-H, Rahnama P and Reitz RD. Progress and recent trends in reactivity-controlled compression ignition engines. *International Journal of Engine Research* 2016; 17: 481–524.
5. Kashdan JT, Docquier N and Bruneaux G. Mixture preparation and combustion via LIEF and LIF of combustion radicals in a direct-injection, HCCI diesel engine. *SAE Technical Paper* 2004; 2004-01-2945.
6. Alriksson M, Rente T and Denbratt I. Low Soot, Low NOx in a Heavy Duty Diesel Engine Using High Levels of EGR. *SAE Technical Paper* 2005; 2005-01-3836.
7. Idicheria CA and Pickett LM. Soot Formation in Diesel Combustion under High-EGR Conditions. *SAE Transactions* 2005; 114: 1559–1574.
8. Andersson Ö and Miles PC. Diesel and diesel LTC combustion. *Encyclopedia of Automotive Engineering* 2014.
9. Yazdani K, Amani E and Naderan H. Multi-objective optimizations of the boot injection strategy for reactivity controlled compression ignition engines. *International Journal of Engine Research* 2019; 20: 889–910.
10. Gordon D, Wouters C, Kinoshita S, et al. Homogeneous charge compression ignition combustion stability improvement using a rapid ignition system. *International Journal of Engine Research* 2020: 1468087420917769.
11. Benajes J, García A, Monsalve-Serrano J, Balloul I and Pradel G. Evaluating the reactivity controlled compression ignition operating range limits in a high-compression ratio medium-duty diesel engine fueled with biodiesel and ethanol. *International Journal of Engine Research* 2017; 18: 66–80.
12. Foucher F, Higelin P, Mounaïm-Rousselle C and Dagaut P. Influence of ozone on the combustion of n-heptane in a HCCI engine. *Proceedings of the Combustion Institute* 2013; 34: 3005–3012.
13. Masurier J-B, Foucher F, Dayma G and Dagaut P. Investigation of iso-octane combustion in a homogeneous charge compression ignition engine seeded by ozone, nitric oxide and nitrogen dioxide. *Proceedings of the Combustion Institute* 2015; 35: 3125–3132.
14. Mangus M, Depcik C, Ragone C and Peltier E. Ozone-Assisted Combustion: Experimental Assessment of the Influence of Ozone in a Single-Cylinder Diesel Engine. In: SAE International, 2015.
15. Bardi M, Pilla G and Matrat M. Experimental Assessment of Ozone Addition Potential in Direct Injection Compression Ignition Engines. *SAE Technical Paper* 2019; 2019-24-0118.
16. Depcik C, Mangus M and Ragone C. Ozone-Assisted Combustion—Part I: Literature Review and Kinetic Study Using Detailed n-Heptane Kinetic Mechanism. *Journal of Engineering for Gas Turbines and Power* 2014; 136, https://doi.org/10.1115/1.4027068 (2014, accessed 8/20/2020).
17. Contino F, Masurier J-B, Foucher F, Lucchini T, D'Errico G and Dagaut P. CFD simulations using the TDAC method to model iso-octane combustion for a large range of ozone seeding and temperature conditions in a single cylinder HCCI engine. *Fuel* 2014; 137: 179–184.
18. Pilla G and Francqueville L de. Investigation of particle formation mechanisms in GDI engines during transient heating operation. *SIA - The Spark Ignition Engine of the Future* 2013.
19. Senecal PK, Richards KJ, Pomraning E, et al. A New Parallel Cut-Cell Cartesian CFD Code for Rapid Grid Generation Applied to In-Cylinder Diesel Engine Simulations. *SAE Technical Paper* 2007; 2007-01-0159.
20. Yakhot V, Orszag SA, Thangam S, Gatski TB and Speziale CG. Development of turbulence models for shear flows by a double expansion technique. *Physics of Fluids A: Fluid Dynamics* 1992; 4: 1510–1520.
21. Amsden AA. KIVA-3V: A block-structured KIVA program for engines with vertical or canted valves 1997.
22. Issa RI, Gosman AD and Watkins AP. The computation of compressible and incompressible recirculating flows by a non-iterative implicit scheme. *Journal of Computational Physics* 1986; 62: 66–82.
23. Payri F, Pastor JV, Pastor JM and Juliá JE. Diesel spray analysis by means of planar laser-induced exciplex fluorescence. *International Journal of Engine Research* 2006; 7: 77–89.
24. XIN J, RICART L and REITZ RD. Computer Modeling of Diesel Spray Atomization and Combustion. *Combustion Science and Technology* 1998; 137: 171–194.
25. Amsden AA, O'Rourke PJ and and Butler TD. KIVA-II: A computer program for chemically reactive flows with sprays 1989, web (1989).
26. Colin O and Benkenida A. The 3-Zones Extended Coherent Flame Model (Ecfm3z) for Computing Premixed/Diffusion Combustion. *Oil & Gas Science and Technology - Rev. IFP* 2004; 59: 593–609.
27. Chevillard S, Colin O, Bohbot J, Wang M, Pomraning E and Senecal PK. Advanced Methodology to Investigate Knock for Downsized Gasoline Direct Injection Engine Using 3D RANS Simulations. *SAE Technical Paper* 2017; 2017-01-0579.
28. Colin O, Pires da Cruz A and Jay S. Detailed chemistry-based auto-ignition model including low temperature phenomena applied to 3-D engine calculations. *Proceedings of the Combustion Institute* 2005; 30: 2649–2656.
29. Bohbot J, Colin O, Velghe A, et al. An Innovative Approach Combining Adaptive Mesh Refinement, the ECFM3Z Turbulent Combustion Model, and the TKI Tabulated Auto-Ignition Model for Diesel Engine CFD Simulations. *SAE Technical Paper* 2016; 2016-01-0604.
30. Mehl M, Pitz WJ, Westbrook CK and Curran HJ. Kinetic modeling of gasoline surrogate components and mixtures under engine conditions. *Proceedings of the Combustion Institute* 2011; 33: 193–200.
31. Masurier J-B, Foucher F, Dayma G and Dagaut P. Homogeneous Charge Compression Ignition Combustion of Primary Reference Fuels Influenced by Ozone Addition. *Energy Fuels* 2013; 27: 5495–5505.
32. Naima K, Liazid A and Bousbaa H. Numerical Simulation of Combustion Behavior of DI Diesel Engine with Conjunction of AMR and Embedding Refinement Strategies. *Combustion Science and Technology* 2018; 2: 112–126.
33. Senecal PK, Pomraning E, Richards KJ and Som S. Grid-Convergent Spray Models for Internal Combustion Engine CFD Simulations. In: *Recht auf Sterbehilfe?: Politische, rechtliche und ethische Positionen*. (ed Niederschlag H and Proft I), Vancouver, BC, Canada, Sept. 23 - 26, 2012, pp. 697–710. Ostfildern: Matthias Grünewald Verlag Schwabenverlag.
34. Bower GR and Foster DE. A Comparison of the Bosch and Zuech Rate of Injection Meters. *SAE Technical Paper* 1991.
35. Dec JE. A Conceptual Model of DI Diesel Combustion Based on Laser-Sheet Imaging. *SAE Transactions* 1997; 106: 1319–1348.
36. Ombrello T, Won SH, Ju Y and Williams S. Flame propagation enhancement by plasma excitation of oxygen. Part I: Effects of O3. *Combustion and Flame* 2010; 157: 1906–1915.
37. Sander SP, Golden DM, Kurylo MJ, et al. Chemical kinetics and photochemical data for use in Atmospheric Studies Evaluation Number 15: JPL Publication 06-2, Jet Propulsion Laboratory, Pasadena, 2006.

38. Atkinson R, Baulch DL, Cox RA, et al. Evaluated kinetic and photochemical data for atmospheric chemistry: Volume I - gas phase reactions of Ox, HOx, NOx and SOx species 2004; 4: 1461–1738.
39. Mansergas A and Anglada JM. The gas-phase reaction between O3 and HO radical: A theoretical study. *Chemphyschem* 2007; 8: 1534–1539.
40. Hatakeyama S and Leu MT. Rate constants for reactions between atmospheric reservoir species. 2. Water. *J. Phys. Chem.* 1989; 93: 5784–5789.
41. R. Atkinson, D. L. Baulch, R. A. Cox, J. N. Crowley, R. F. Summary of Evaluated Kinetic and Photochemical Data for Atmospheric Chemistry: Web version 2001.
42. Atkinson R, Baulch DL, Cox RA, Hampson RF, Kerr JA and Troe J. Evaluated Kinetic and Photochemical Data for Atmospheric Chemistry: Supplement III. IUPAC Subcommittee on Gas Kinetic Data Evaluation for Atmospheric Chemistry. *Journal of Physical and Chemical Reference Data* 1989; 18: 881–1097.
43. Howard CJ and Finlayson-Pitts BJ. Yields of HO 2 in the reaction of hydrogen atoms with ozone. *The Journal of Chemical Physics* 1980; 72: 3842–3843.
44. Starik AM, Kozlov VE and Titova NS. On the influence of singlet oxygen molecules on the speed of flame propagation in methane–air mixture. *Combustion and Flame* 2010; 157: 313–327.

9 Appendix 1: O₃ block reaction mechanism (form : $k = AT^n e^{-\frac{E_a}{RT}}$)

Reaction	A	n	E$_a$	Reference
O3+N2=>O2+O+N2	4.00E+14	0	22667	36
O2+O+N2=>O3+N2	1.60E+14	-0.4	-1391	36
O3+O2=>O2+O+O2	1.54E+14	0	23064	36
O2+O+O2=>O3+O2	3.26E+19	-2.1	0	36
O3+O3=>O2+O+O3	4.40E+14	0	23064	36
O2+O+O3=>O3+O3	1.67E+15	-0.5	-1391	36
O3+H<=>O2+OH	8.43E+13	0	934	37
O3+O<=>O2+O2	4.82E+12	0	4094	38
O3+OH<=>O2+HO2	1.85E+11	0	831	39
O3+HO2<=>O2+OH+O2	6.02E+09	0	938	37
O3+H2O<=>O2+H2O2	6.62E+01	0	0	40
O3+CH3<=>O2+CH3O	3.07E+12	0	417	41
O3+NO<=>O2+NO2	8.43E+11	0	2603	38
O3+N<=>O2+NO	6.03E+07	0	0	42
O3+H<=>O+HO2	4.52E+11	0	0	43
O3+H2<=>OH+HO2	6.00E+10	0	19840	44
O3+CH4<=>CH3O+HO2	8.13E+10	0	15280	44
N+NO<=>N2+O	2.70E+13	0	355	
N+O2<=>NO+O	9.00E+09	1	6500	
N+OH<=>NO+H	3.36E+13	0	385	
N2O+O<=>N2+O2	1.40E+12	0	10810	
N2O+O<=>2NO	2.90E+13	0	23150	
N2O+H<=>N2+OH	3.87E+14	0	18880	
N2O+OH<=>N2+HO2	2.00E+12	0	21060	
N2O(+M)<=>N2+O(+M)	7.91E+10	0	56020	
HO2+NO<=>NO2+OH	2.11E+12	0	-480	
NO+O+M<=>NO2+M	1.06E+20	-1.41	0	
NO2+O<=>NO+O2	3.90E+12	0	-240	
NO2+H<=>NO+OH	1.32E+14	0	360	
NH+O<=>NO+H	4.00E+13	0	0	
NH+H<=>N+H2	3.20E+13	0	330	
NH+OH<=>HNO+H	2.00E+13	0	0	
NH+OH<=>N+H2O	2.00E+09	1.2	0	
NH+O2<=>HNO+O	4.61E+05	2	6500	
NH+O2<=>NO+OH	1.28E+06	1.5	100	
NH+N<=>N2+H	1.50E+13	0	0	
NH+H2O<=>HNO+H2	2.00E+13	0	13850	
NH+NO<=>N2+OH	2.16E+13	-0.23	0	
NH+NO<=>N2O+H	3.65E+14	-0.45	0	
NH2+O<=>OH+NH	3.00E+12	0	0	
NH2+O<=>H+HNO	3.90E+13	0	0	
NH2+H<=>NH+H2	4.00E+13	0	3650	
NH2+OH<=>NH+H2O	9.00E+07	1.5	-460	
NNH<=>N2+H	3.30E+08	0	0	
NNH+M<=>N2+H+M	1.30E+14	-0.11	4980	
NNH+O2<=>HO2+N2	5.00E+12	0	0	
NNH+O<=>OH+N2	2.50E+13	0	0	
NNH+O<=>NH+NO	7.00E+13	0	0	
NNH+H<=>H2+N2	5.00E+13	0	0	
NNH+OH<=>H2O+N2	2.00E+13	0	0	
NNH+CH3<=>CH4+N2	2.50E+13	0	0	
H+NO+M<=>HNO+M	4.48E+19	-1.32	740	
HNO+O<=>NO+OH	2.50E+13	0	0	
HNO+H<=>H2+NO	9.00E+11	0.72	660	
HNO+OH<=>NO+H2O	1.30E+07	1.9	-950	
HNO+O2<=>HO2+NO	1.00E+13	0	13000	
CN+O<=>CO+N	7.70E+13	0	0	
CN+OH<=>NCO+H	4.00E+13	0	0	
CN+H2O<=>HCN+OH	8.00E+12	0	7460	
CN+O2<=>NCO+O	6.14E+12	0	-440	
CN+H2<=>HCN+H	2.95E+05	2.45	2240	
NCO+O<=>NO+CO	2.35E+13	0	0	
NCO+H<=>NH+CO	5.40E+13	0	0	
NCO+OH<=>NO+H+CO	2.50E+12	0	0	
NCO+N<=>N2+CO	2.00E+13	0	0	
NCO+O2<=>NO+CO2	2.00E+12	0	20000	
NCO+M<=>N+CO+M	3.10E+14	0	54050	
NCO+NO<=>N2O+CO	1.90E+17	-1.52	740	
NCO+NO<=>N2+CO2	3.80E+18	-2	800	
HCN+M<=>H+CN+M	1.04E+29	-3.3	126600	

HCN+O<=>NCO+H	2.03E+04	2.64	4980
HCN+O<=>NH+CO	5.07E+03	2.64	4980
HCN+O<=>CN+OH	3.91E+09	1.58	26600
HCN+OH<=>HOCN+H	1.10E+06	2.03	13370
HCN+OH<=>HNCO+H	4.40E+03	2.26	6400
HCN+OH<=>NH2+CO	1.60E+02	2.56	9000
H+HCN(+M)<=>H2CN(+M)	3.30E+13	0	0
H2CN+N<=>N2+CH2	6.00E+13	0	400
C+N2<=>CN+N	6.30E+13	0	46020
CH+N2<=>HCN+N	3.12E+09	0.88	20130
CH+N2(+M)<=>HCNN(+M)	3.10E+12	0.15	0
CH2+N2<=>HCN+NH	1.00E+13	0	74000
CH2(S)+N2<=>NH+HCN	1.00E+11	0	65000
C+NO<=>CN+O	1.90E+13	0	0
C+NO<=>CO+N	2.90E+13	0	0
CH+NO<=>HCN+O	4.10E+13	0	0
CH+NO<=>H+NCO	1.62E+13	0	0
CH+NO<=>N+HCO	2.46E+13	0	0
CH2+NO<=>H+HNCO	3.10E+17	-1.38	1270
CH2+NO<=>OH+HCN	2.90E+14	-0.69	760
CH2+NO<=>H+HCNO	3.80E+13	-0.36	580
CH2(S)+NO<=>H+HNCO	3.10E+17	-1.38	1270
CH2(S)+NO<=>OH+HCN	2.90E+14	-0.69	760
CH2(S)+NO<=>H+HCNO	3.80E+13	-0.36	580
CH3+NO<=>HCN+H2O	9.60E+13	0	28800
CH3+NO<=>H2CN+OH	1.00E+12	0	21750
HCNN+O<=>CO+H+N2	2.20E+13	0	0
HCNN+O<=>HCN+NO	2.00E+12	0	0
HCNN+O2<=>O+HCO+N2	1.20E+13	0	0
HCNN+OH<=>H+HCO+N2	1.20E+13	0	0
HCNN+H<=>CH2+N2	1.00E+14	0	0
HNCO+O<=>NH+CO2	9.80E+07	1.41	8500
HNCO+O<=>HNO+CO	1.50E+08	1.57	44000
HNCO+O<=>NCO+OH	2.20E+06	2.11	11400
HNCO+H<=>NH2+CO	2.25E+07	1.7	3800
HNCO+H<=>H2+NCO	1.05E+05	2.5	13300
HNCO+OH<=>NCO+H2O	3.30E+07	1.5	3600
HNCO+OH<=>NH2+CO2	3.30E+06	1.5	3600
HNCO+M<=>NH+CO+M	1.18E+16	0	84720
HCNO+H<=>H+HNCO	2.10E+15	-0.69	2850
HCNO+H<=>OH+HCN	2.70E+11	0.18	2120
HCNO+H<=>NH2+CO	1.70E+14	-0.75	2890
HOCN+H<=>H+HNCO	2.00E+07	2	2000
HCCO+NO<=>HCNO+CO	9.00E+12	0	0
CH3+N<=>H2CN+H	6.10E+14	-0.31	290
CH3+N<=>HCN+H2	3.70E+12	0.15	-90
NH3+H<=>NH2+H2	5.40E+05	2.4	9915
NH3+OH<=>NH2+H2O	5.00E+07	1.6	955
NH3+O<=>NH2+OH	9.40E+06	1.94	6460
NH+CO2<=>HNO+CO	1.00E+13	0	14350
CN+NO2<=>NCO+NO	6.16E+15	-0.752	345
NCO+NO2<=>N2O+CO2	3.25E+12	0	-705
N+CO2<=>NO+CO	3.00E+12	0	11300